Pendellösung Fringes in Stroboscopic X-ray Section Topography of Weakly Excited Quartz Resonators

By Y. Zheng, A. Zarka and B. Capelle

Laboratoire de Minéralogie-Cristallographie, Universités P. & M. Curie (Paris VI) et Paris VII, unité associée au CNRS, 4 Place Jussieu, 75252 Paris CEDEX 05, France

and J. Detaint and J. Schwartzel

Centre National d'Etudes des Télécommunications, PAB/BAG/MCT, 92220 Bagneux, France

Abstract

The theory for slightly distorted crystals [Kato (1963). *J. Phys. Soc. Jpn*, **18**, 1785-1791] is applied to the case of quartz AT-cut resonators to interpret stroboscopic section topographs. Features in the diffraction process such as ray trajectories, phase changes and intensities of diffracted waves are drawn from this theory. Furthermore, it is shown that extra *Pendellösung* fringes appearing on section topographs with increasing acoustic vibration can be directly related to the vibration amplitude within a precision of about 0·3 Å. Experimental images are compared with Kato's theoretical profiles and simulated images obtained by solving Takagi's [*Acta Cryst.* (1962), **15**, 1311-1312] equations. The results lead to the conclusion that stroboscopic X-ray topography is a precise method to measure the vibration amplitude in weakly excited resonators.

1. Introduction

Takagi's equations provide global solutions for X-ray waves in any distorted crystal (Takagi, 1962, 1969; Taupin, 1964). Nevertheless, this approach is complicated and does not involve classical notions of geometrical optics which are helpful in the understanding of the diffraction process. The theory developed by Penning & Polder (1961) and Kato (1963, 1964) for slightly distorted crystals appears to be very useful for our purpose. This theory was applied to the case of bent crystals and revealed that extra fringes are expected on section topographs with increasing strain gradient, in perfect agreement with experimental results (Kato & Ando, 1966; Ando & Kato, 1966; Hart, 1966).

In this paper, Kato's theory for crystals under slight thickness shear is developed and it is shown that extra fringes appear, similarly to the case of bent crystals, with increasing amplitude of the acoustic vibration. Experimental section topographs using the stroboscopic technique are shown and permit a comparison

with profiles calculated from Kato's theory and with simulated images obtained by solving Takagi's equations.

It is interesting to point out here that several different approaches for X-ray, γ-ray and neutron diffraction in crystals submitted to an acoustic wave have been proposed by several authors (Kohler, Mohling & Peibst, 1974; Dyublik, 1986; Polikarpov & Skadorv, 1987). These approaches, which were developed for the plane-wave case, are based on the fact that a crystal within an acoustic wave can be described by a superlattice combining the crystal periodicity and the acoustic periodicity.

2. Diffraction theory

In this section, Kato's theory for slightly distorted crystals is summarized (Kato, 1963, 1964, 1974). For the sake of simplicity, expressions are written for the symmetric Laue case and for diffracted waves only. The axes used are presented in Fig. 1 where the X-ray point source, denoted by *o* on the entrance face, is taken as the origin. When an X-ray beam enters a slightly distorted crystal, two kinds of modified Bloch waves are excited. The trajectory of the modified
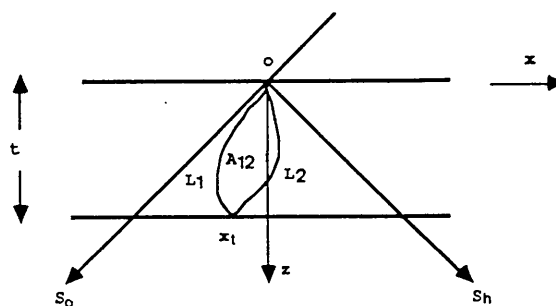

Fig. 1. Diffraction geometry. *o*: X-ray point source; s_o and s_h: incident and diffracted directions respectively; L_1 and L_2: trajectories ending at the point x_t on the exit face; A_{12}: area limited by L_1 and L_2.

Bloch wave obeys the equation

$$\pm m_o \frac{d}{dz} \frac{p}{(1-p^2)^{1/2}} = f(x, z) \qquad (2.1)$$

where the upper and lower signs correspond respectively to the upper and lower branches of the dispersion surface. These two families of trajectories are called here wavefield (1) and wavefield (2) respectively. The quantity m_o is related to the extinction distance Λ_o by $m_o = \pi/\Lambda_o c$ where $c = \tan \theta_B$ and θ_B is the Bragg angle. p, called here the trajectory inclination, is the gradient of the trajectory $\tan \theta = dx/dz$ normalized by c: $p = \tan \theta/c$, so that $p = \pm 1$ indicate the directions of the Borrmann triangle edges and $p = 0$ indicates the oz direction. The term $f(x, z)$ is called the 'force' and is expressed in term of the displacement vector $\mathbf{u}(\mathbf{r})$:

$$f(x, z) = \pi \left\{ \frac{1}{c} \frac{\partial^2}{\partial z^2} - c \frac{\partial^2}{\partial x^2} \right\} \mathbf{h} \cdot \mathbf{u} \qquad (2.2)$$

where $\mathbf{h}$ represents the reflection vector.

Two waves arriving at any point on the exit face interfere and the total intensity is therefore given by

$$I = [B_1 I_1 + B_2 I_2 + 2(I_1 I_2)^{1/2} \cos (S)]$$

$$\times \exp (-\mu_o t/\cos \theta_B). \qquad (2.3)$$

I_i are the intensities of diffracted waves in the nonabsorption case; the absorption effect is introduced by B_i, which describes the anomalous absorption effect, and the exponential term for the ordinary photoelectric absorption effect where μ_o is the linear absorption factor (Appendix I). The important term is S, the phase difference between the two wavefields, which determines the *Pendellösung* fringe contour. In particular, the positions of nth-order fringes are given by the condition $S = 2n\pi$. The expression for the phase difference is

$$S = -\pi/2 + T + N$$

$$= -\pi/2 + m_o c \int_{L_1+L_2} (1-p^2)^{1/2} dz$$

$$+ \int_{A_{12}} f(x, z) dx dz \qquad (2.4)$$

where the term $-\pi/2$ is the intrinsic phase difference between wavefield (1) and wavefield (2) specific to the spherical form of the incident beam. In the first integral T, called the kinetic term, L_1 and L_2 denote the trajectories of the two wavefields respectively. The second integral N is called the potential term where A_{12} is the area limited by L_1 and L_2. In this integral, the area A_{12} is counted positively when the circuit L_1-L_2 limiting A_{12} is clockwise.

The validity criterion of this theory is qualitative. The radius of curvature should not be so small that the direction of propagation of the wavefields changes from that of the reflected wave to that of the incident

wave in a quarter of an extinction distance:

$$\tfrac{1}{4}\langle(1-p^2)\rangle \left| \left\{ \frac{\partial^2}{\partial z^2} - c^2 \frac{\partial^2}{\partial x^2} \right\} \mathbf{h} \cdot \mathbf{u} \right| \Lambda_o^2 \leq 1 \qquad (2.5)$$

where $\langle \ \rangle$ indicates the average value along one trajectory. This is equivalent to the usual criterion for non-interbranch scattering in X-ray dynamical theory (Balibar, 1968).

3. Case of a crystal under pure thickness shear

An ideal case where the acoustic vibration is a pure cosine wave of thickness-shear mode is considered here:

$$u(z) = u_o \cos (n\pi z/t) \qquad (3.1)$$

where the displacement u is along the ox axis, *i.e.* parallel to the reflection vector $\mathbf{h}$ for the symmetric Laue case, u_o is the vibration amplitude, n an odd number and t the crystal thickness. The acoustic wavelength L_o is related to the thickness by $L_o = 2t/n$. To illustrate the following calculations, the values used are taken from the case of a quartz AT-cut crystal. The values concerning the acoustic characteristics are $n = 5$, $t = 1\cdot3196$ mm ($L_o = 0\cdot52784$ mm), and the diffraction values are the reflection vector $\mathbf{h} = 2\bar{1}0$, lattice distance $d_o = 1/h = 2\cdot45655$ Å and extinction distance along the reflection plane $\Lambda_o = 101\cdot6$ μm which corresponds to an X-ray wavelength of $0\cdot689$ Å.

The validity criterion (2.5) applied to the present case gives

$$\tfrac{1}{4}\langle(1-p^2)\rangle(1/d_o)|d^2u/dz^2|\Lambda_o^2 \leq (u_o/4d_o)(n\pi/t)^2\Lambda_o^2$$

$$\leq 1$$

or

$$u_o/d_o \leq (1/\pi^2)(L_o/\Lambda_o)^2. \qquad (3.2)$$

This means that the theory is applicable for the range of $u_o \leq 7$ Å. For the sake of convenience, the following discussion concerns the range of $u_o \leq 5$ Å and its extension is quite easy.

(A) Trajectories

From (2.2), the force $f(z)$ is obtained and it varies only with thickness for the present case, in the same way as the displacement $u(z)$:

$$f(z) = \frac{\pi}{c} \frac{d^2 \mathbf{h} \cdot \mathbf{u}}{dz^2}$$

$$= -\frac{\pi}{c} \frac{u_o}{d_o} (n\pi)^2 \frac{1}{t^2} \cos \left(n\pi \frac{z}{t} \right). \qquad (3.3)$$

The trajectory is integrated from (2.1):

$$\frac{x}{ct} = \int_0^{z/t} \frac{a \mp b \sin (n\pi\varphi)}{\{1 + [a \mp b \sin (n\pi\varphi)]^2\}^{1/2}} d\varphi. \qquad (3.4)$$

The parameter a is related to the initial inclination p_e at the entrance point of a trajectory, $a = p_e/(1 - p_e^2)^{1/2}$, and it is called the trajectory parameter. b is the ratio between the acoustic characteristics u_o/L_o and the diffraction ones d_o/Λ_o: $b = 2\pi u_o \Lambda_o/d_o L_o$. The integral (3.4) could in principle be expressed in terms of elliptic integrals in a rather complicated way which will not simplify our discussion, so the trajectory equation will be left in this integral form; its calculation is very easy. Some properties of trajectories can be deduced from (3.4) (Appendix II):

(α) The trajectories of one wavefield do not cross each other. This point was taken into account in (2.4) for phase S, since phase jumps should be added to S in the case of crossing trajectories.

(β) The inclination of a trajectory at the exit face ($z = t$) is the same as that at the entrance face ($z = 0$).

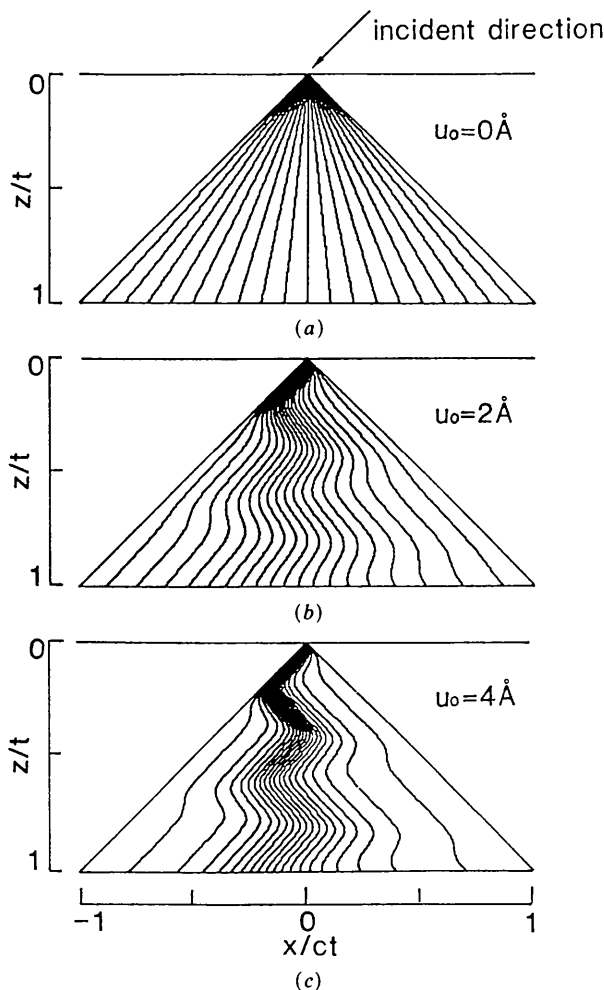(γ) Trajectories of wavefield (1) and wavefield (2)

Fig. 2. Selected trajectories. The trajectory inclinations at the entrance point are the same for the three cases: p_e varies from -1 to 1 with step 0.1. (a) $u_o = 0$ Å, perfect crystal; (b) $u_o = 2$ Å; (c) $u_o = 4$ Å.

are symmetric with respect to the oz axis. More precisely, if a trajectory L_1 of wavefield (1) is defined by the initial inclination $+p_e$ (or $+a$), the trajectory L_2 of wavefield (2), defined by the opposite initial inclination $-p_e$ (or $-a$), is symmetric with respect to the oz axis. This symmetry exists also for the intensities of two wavefields, as will be shown later.

Trajectories of wavefield (1) with different initial inclinations p_e are shown in Figs. 2(a)-(c), corresponding respectively to $u_o = 0, 2$ and 4 Å. In comparison with hyperbolic trajectories in a homogeneously bent crystal, trajectories in the present case have an oscillating form related to the form of the acoustic wave. As the vibration increases, these trajectories converge to a region around the middle of the Borrmann triangle and shifted to the side of the incident beam. Because of the symmetry, the corresponding trajectories of wavefield (2) are of the same form and converge to the side of the diffracted beam. The contraction of the trajectories on the central part constitutes one factor contributing to the increase of diffracted intensity with increasing vibration amplitude.

The asymptotic expression of the trajectories [wavefield (1)] close to the edges of the Borrmann triangle ($a \to \pm\infty$ or $p_e \to \pm1$) can be calculated as

$$\frac{x}{ct} = \pm\frac{z}{t}\left(1 - \frac{1}{2a^2}\right) \pm \frac{b}{a^3}\frac{\cos(n\pi z/t) - 1}{n\pi}$$

$$\text{for } a \to \pm\infty \qquad (3.5)$$

where the first term $\pm(z/t)(1 - 1/2a^2)$ corresponds to the straight trajectory for the perfect crystal and the second interprets the influence of the acoustic vibration on the trajectory. The trajectories with the initial inclination $p_e = 0$ (or $a = 0$) also have a simple expression:

$$x/ct = (1/n\pi)(\arcsin\{[b/(1 + b^2)^{1/2}]\cos(n\pi z/t)\}$$

$$- \arcsin[b/(1 + b^2)^{1/2}]). \qquad (3.6)$$

(B) Intensities

For any point x_t on the exit face, the parameters a_1 and a_2 of the two trajectories ending at this point can be determined from the trajectory equation (3.4) by putting $x(z = t) = x_t$. The intensity of diffracted waves (normalized by the energy of the incident spherical wave) without the absorption effect is thus expressed in term of the parameters a_1 and a_2 (Appendix III):

$$I_i = (\pi/4\Lambda_o t \sin^2\theta_B)\{(1 + a_i^2)$$

$$\times \int_0^1 (1 + [a_i \mp b\sin(n\pi\varphi)]^2)^{-3/2}\,d\varphi\}^{-1} \qquad (3.7)$$

where a_1 and the upper sign are attributed to wavefield (1) and a_2 and the lower sign to wavefield (2).

The intensities of wavefields (1) and (2) are symmetric with respect to the oz axis (the middle of the Borrmann triangle). In Fig. 3 the intensity of wavefield (1) along the exit face for different vibration amplitudes is shown. When the vibration increases, the intensity is mostly increased in the vicinity of the central point along the exit face on the side of the incident beam. As the same increase occurs for wavefield (2) symmetrically on the side of the diffracted beam, an increase of the total intensity is expected on the central part of experimental section topographs.

(C) Phase and total intensity

Similarly, the phase difference between two waves arriving at any point of the exit face can be deduced from (2.3) as a function of the parameters a_1 and a_2 of the two trajectories. The kinetic term and the potential term have the following expressions:

$$T = (\pi t / \Lambda_o) \int_0^1 (\{1 + [a_1 - b \sin (n\pi\varphi)]^2\}^{-1/2}$$

$$+ \{1 + [a_2 + b \sin (n\pi\varphi)]^2\}^{-1/2}) \, d\varphi \qquad (3.8)$$

$$N = \int_{A_{12}} f(z) \, dx \, dz$$

$$= (\pi t / \Lambda_o) \int_0^t \{[x_1(z) - x_2(z)]/ct\}$$

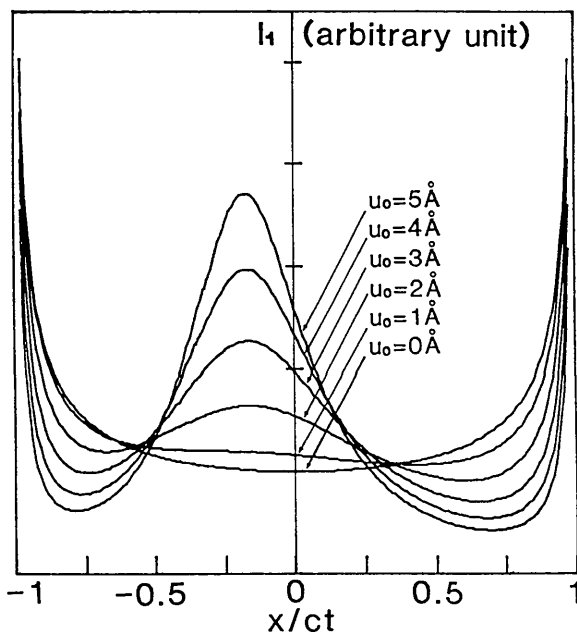$$\times b \cos (n\pi z/t) n\pi \, dz/t \qquad (3.9)$$

where x_1 and x_2 refer to the trajectories which limit the area A_{12} and belong respectively to wavefield (1) and wavefield (2).

The variation of $T/2\pi$, $N/2\pi$ and $S/2\pi$ along the exit face are shown in Fig. 4 for different vibration amplitudes. It is recalled here that each integer number for $S/2\pi$ corresponds to a maximum in *Pendellösung* fringes. For the perfect crystal ($u_o = 0$ Å), $S/2\pi$ increases from the edges of the Borrmann triangle to the central point up to the value of 12·7, i.e. 12 *Pendellösung* fringes are expected. When the vibration amplitude increases from 0 to 5 Å, the kinetic term T decreases and the potential term N, which is mostly connected to the displacement field by the force term $f(x, z)$, increases very quickly. Then the total phase difference $S/2\pi$ increases up to 24·2 and this means that 12 extra *Pendellösung* fringes are expected with a vibration amplitude of 5 Å. The total intensity (2.3) is plotted in Fig. 5 for different values of u_o where the anomalous absorption B_i is neglected for its very small influence on the fringe positions. The fringe spacing (Fig. 5) along the exit face is directly related to the phase change (Fig. 4c). The higher the vibration amplitude, the more rapidly the phase increases away from the edges of the Borrmann triangle. Fringe spacing reduces very rapidly at the edges. But at the central point along the exit face, the phase reaches its maximal value and it changes relatively slowly, so that the fringe spacing remains essentially the same. This remark suggests that under vibration only large spacing fringes on the central part of section topographs could be resolved experimentally.

(D) Relation between extra fringes and vibration amplitude

The fine structure of *Pendellösung* fringes near the edges of the Borrmann triangle can rarely be resolved experimentally and, as was pointed out previously, the situation becomes still more emphasized with the presence of an acoustic vibration. To relate extra fringes to the vibration amplitude, the central part of section topographs is studied. More precisely the intensity and phase at the central point along the exit face are calculated as a function of u_o. All the expressions remain the same as previously, with in addition the simplification that the two trajectories ending at the central point have opposite initial inclinations p_e (or a): $a_1 = -a_2$. a_1 is denoted here by $a_o(b)$. The parameter $a_o(b)$ is determined from (3.4) by putting $x(z = t) = 0$ for the trajectory of wavefield (1).

The intensities and phase of the waves are related to the vibration amplitude through the function $a_o(b)$. Fig. 6 shows the dependence of the intensities of the two wavefields $I_o(= I_1 = I_2)$ on the vibration amplitude u_o. The intensity of diffracted waves is increased by a factor of 2·5 at the central point along the exit

Fig. 3. Intensity I_1 of wavefield (1) along the exit face for different vibration amplitudes.

face, when the vibration amplitude u_o increases from 0 to 5 Å.

Similarly, the expression of the phase difference is rewritten in terms of $a_o(b)$ from (3.8) and (3.9) as

$$T = (2\pi t/\Lambda_o) \int_0^1 \{1 + [a_o(b) - b \cos(n\pi\varphi)]^2\}^{-1/2} \, d\varphi \qquad (3.10)$$

$$N = (2\pi t/\Lambda_o) \int_0^1 \int_0^\varphi \frac{a_o(b) - b \sin(n\pi\phi)}{\{1 + [a_o(b) - b \sin(n\pi\phi)]^2\}^{1/2}} \, d\phi$$

$$\times \, b \cos(n\pi\varphi) n\pi \, d\varphi$$

$$= (2\pi t/\Lambda_o) \int_0^1 \frac{a_o(b) - b \sin(n\pi\varphi)}{\{1 + [a_o(b) - b \sin(n\pi\varphi)]^2\}^{-1/2}}$$

$$\times \, [-b \sin(n\pi\varphi)] \, d\varphi$$

$$= (2\pi t/\Lambda_o) \int_0^1 \{1 + [a_o(b) - b \sin(n\pi\varphi)]^2\}^{1/2}$$

$$- \{1 + [a_o(b) - b \sin(n\pi\varphi)]^2\}^{-1/2} \, d\varphi. \qquad (3.11)$$

The total phase difference $S(=-\pi/2 + T + N)$ is then

$$S = -\pi/2 + (2\pi t/\Lambda_o)$$

$$\times \int_0^1 \{1 + [a_o(b) - b \sin(n\pi\varphi)]^2\}^{1/2} \, d\varphi. \qquad (3.12)$$

The variations of $T/2\pi$, $N/2\pi$ and $S/2\pi$ as functions of u_o are plotted in Fig. 7, which shows again that at the central point along the exit face $S/2\pi$ increases from 12·7 to 24·2 when u_o varies from 0 to 5 Å, i.e. 12 extra fringes are expected.

The total intensity, with the anomalous absorption effect B_i neglected, is obtained from (2.3) (Fig. 8):

$$I = 2I_o[1 + \cos(S)] \exp(-\mu_o t/\cos \theta_B). \qquad (3.13)$$

This curve shows that the number of extra fringes appearing on section topographs is a very sensitive indication of the vibration amplitude range. This relation constitutes our basic tool to correlate extra fringes to the vibration amplitude for the following real cases.

4. Samples, results and discussion

(A) Resonator geometry and deformation model

The resonators studied are synthetic quartz AT-cut plano-convex ones (Fig. 9). The diameters of the crystal plates (D_1) and of the metallic electrodes (D_2) are 15 and 8 mm respectively. The upper face of the plates has a curved form in order to confine the acoustic energy under the electrodes and the curvature radius R is 175 mm. The crystal thickness $t(x, y)$ at any point on the plates is determined by the maximal thickness $t_0(=1\cdot3196 \text{ mm})$ at the centre of the plates and the curvature radius R:

$$t(x, y) = t_o - R + [R^2 - (x^2 + y^2)]^{1/2}. \qquad (4.1)$$

The total thickness variation in this case is about 160 μm which implies the existence of one or two supplementary fringes due to the thickness variation $(\Lambda_o = 101\cdot6 \text{ μm})$, even without vibration.

For thickness shear modes, the piezoelectric effect implies essentially a displacement u_x along the x axis. This displacement u_x, denoted here as $u(\mathbf{r})$, can be decomposed into the eigenmodes which are described by three integer numbers (n, m, p) related to the boundary conditions along the oz, ox and oy directions respectively (Tiersten & Smythe, 1979; Stevens & Tiersten, 1986):

$$u(\mathbf{r}) = \left[-\frac{e_{22}}{c_{66}} \frac{Vz}{t(x, y)} + \sum_{nmp} C^{nmp} u_{nmp}(\mathbf{r}) \right] \exp(-i\omega t) \qquad (4.2)$$
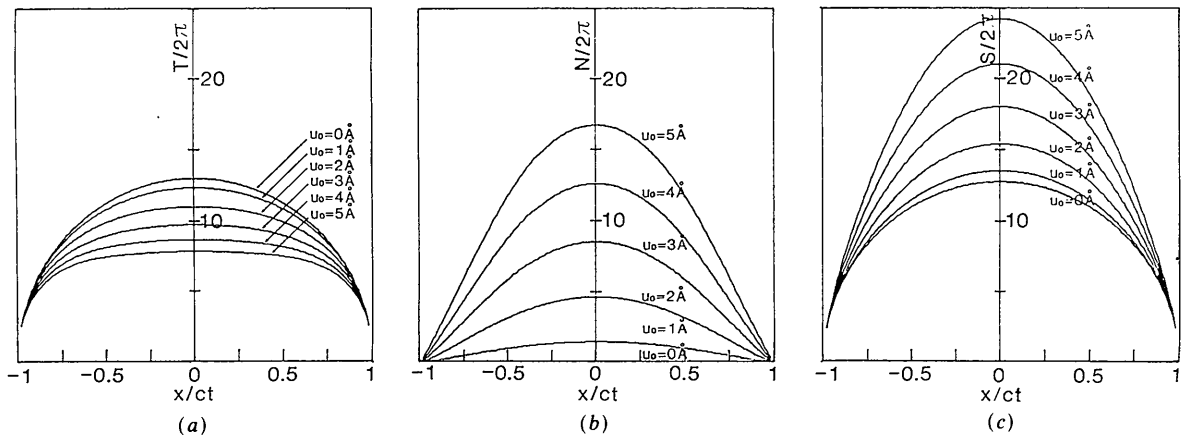

Fig. 4. Phase difference along the exit face for different vibration amplitudes. (a) $T/2\pi$, kinetic term; (b) $N/2\pi$, potential term; (c) $S/2\pi$, total phase.
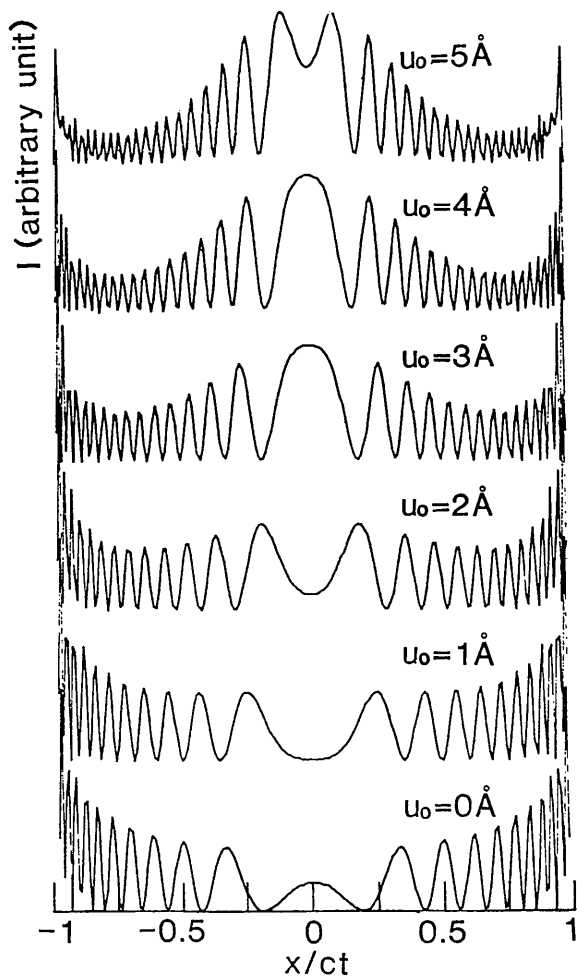
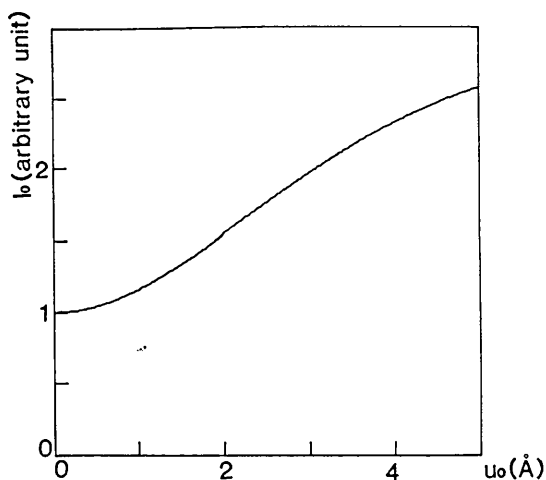Fig. 5. Total intensity of diffracted waves along the exit face for different vibration amplitudes.
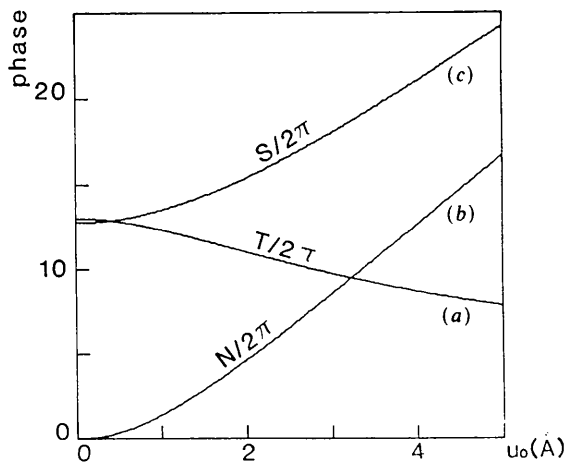

Fig. 7. Phase difference at the central point along the exit face with increasing vibration amplitude. (*a*) $T/2\pi$, kinetic term; (*b*) $N/2\pi$, potential term; (*c*) $S/2\pi$, total phase.
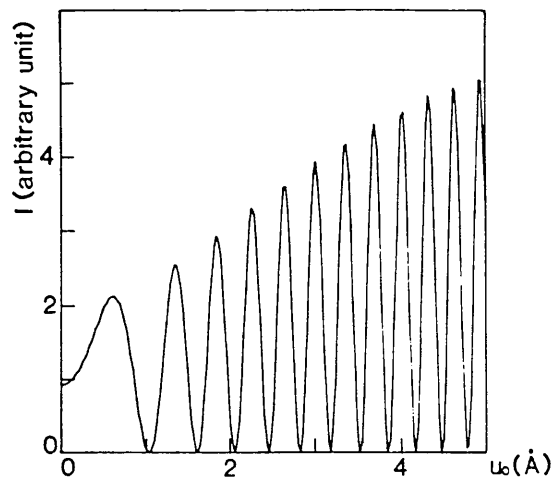

Fig. 8. Total intensity of diffracted waves at the central point along the exit face with increasing vibration amplitude.
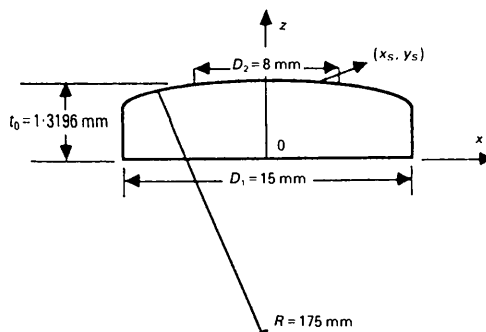

Fig. 6. Intensity $I_o(=I_1=I_2)$ of wavefield (1) or wavefield (2) at the central point along the exit face with increasing vibration amplitude.

Fig. 9. Resonator geometry. t_o: maximal thickness; D_1: resonator diameter; D_2: electrode diameter; R: curvature radius; (x_s, y_s): symbolic point of an incident beam arriving at the resonator surface.

where $u_{nmp}(\mathbf{r})$ represents the (n, m, p) eigenmode displacement with a conventionally adopted form and C^{nmp} is the component of $u(\mathbf{r})$ decomposed on the (n, m, p) mode. The first term in (4.2) interprets simply the driving piezoelectric effect. In the notation usually employed, the number n is an odd one indicating the number of nodal planes in thickness and m and p are even numbers indicating the number of local minima in the amplitude envelopes along the ox and oy directions respectively. When one particular (n, m, p) mode is at resonance, $u(\mathbf{r})$ can be simply approximated by the resonant mode $C^{nmp}u_{nmp}(\mathbf{r})$. In particular, the mode $(n, m, p) = (5, 0, 0)$ considered experimentally has the expression

$$u = u_o \exp[-(\alpha_5 x^2 + \beta_5 y^2)/2]$$
$$\times \cos[5\pi z/t(x, y)] \exp(-i\omega t), \quad (4.3)$$

where α_5 and β_5 are amplitude attenuation coefficients determined by the piezoelectric–elastic constants and geometry factors such as t_o and R. In our case, $\alpha_5 = 0.445297 \text{ mm}^{-2}$ and $\beta_5 = 0.509546 \text{ mm}^{-2}$ and this means that the vibration amplitude is attenuated from the centre to the electrode edge $(x^2 + y^2 = 4^2 \text{ mm}^2)$ by a factor of about 2.8×10^{-2}. The vibration amplitude u_o at the centre of the resonator is related to the excitation voltage V and to the departure of the driving frequency ω from the resonance frequency ω_{500}:

$$u_o = \text{constant} \times V/(1 - \omega_{500}^2/\omega^2). \quad (4.4)$$

In this formulation where energy dissipation is neglected, u_o becomes infinite at the resonance. The energy dissipation effect near the resonance is introduced empirically by putting in a resistive part in analogy with electrical circuits:

$$\omega'_{500} = \omega_{500} + i\omega_{500}/2Q \quad (4.5)$$

where Q, the quality factor, is of order of 1×10^6 for our resonators in a room environment. If we take into account this hypothesis in (4.4), the vibration amplitude u_o is proportional to the excitation voltage V and the quality factor Q at/near the resonance:

$$u_o = \text{constant} \times VQ. \quad (4.6)$$

As an example, an applied voltage of about 5 mV corresponds to an amplitude u_o of about 4.9 Å.

(B) Experimental method

The stroboscopic experiments using synchrotron radiation were performed at LURE (Orsay, France) with the storage ring of DCI (Zarka, Capelle, Detaint & Schwartzel, 1987). This method is very well adapted to study resonators because the thickness shear resonance frequency and the frequency of the pulsed radiation are of the same order (MHz). For our cases, the resonators were shaped in such a way that

the $(5, 0, 0)$ mode frequency is twice the pulsed synchrotron-radiation frequency $(\omega_{500}/2\pi = 2 \times 3.169280 \text{ MHz})$. The electrical excitation on the resonator is derived from the radiation pulse signal, so that the crystal is forced to vibrate at the resonance frequency and in synchronism with the radiation pulse. Further, a phase shifter permits regulation of the relative time phase between the radiation pulse and the vibration, i.e. one may observe the vibration at different stages resolved in a 1 ns time. The slit limiting the incident beam was about 15 μm wide and the Laue setting was used because it permits several images of different reflections to be obtained simultaneously. The crystals were set with a Bragg angle θ_B of 8.068°, so that the selected incident X-ray wavelength λ for the $2\bar{1}0$ reflection was about 0.689 Å.

(C) Intensity profiles

If (x_s, y_s) denotes the position of a point source on the upper face of the resonator (Fig. 9), the displacement $u(\mathbf{r})$ can be transformed into the diffraction axis set (Fig. 1). Further, under stroboscopic experiments, the displacement $u(\mathbf{r})$ appears to be fixed and has an apparent amplitude $u_o \cos \Phi$, where Φ is the relative time phase between the vibration and the pulsed radiation. The apparent displacement $u'(\mathbf{r})$ in the diffraction plane is thus

$$u' = u_o \cos \Phi \exp\{-[\alpha_5(x + x_s)^2 + \beta_5 y_s^2]/2\}$$
$$\times \cos[5\pi z/t(x + x_s, y_s)]$$

or

$$u' = \exp[-\alpha_5(x^2 + 2x_s x)/2]u_o(x_s, y_s)$$
$$\times \cos[5\pi z/t(x + x_s, y_s)] \quad (4.7)$$

where $u_o(x_s, y_s) = u_o \cos \Phi \exp[-(\alpha_5 x_s^2 + \beta_5 y_s^2)/2]$ is the vibration amplitude at the entrance point. The vibration amplitude and the crystal thickness depend on x and are not constant inside the Borrmann triangle. These variations can be neglected here because they are small over the Borrmann triangle. By inserting the values at the entrance point (x_s, y_s), one may obtain an approximate expression for $u'(\mathbf{r})$:

$$u' \simeq u_o(x_s, y_s) \cos[5\pi z/t(x_s, y_s)]. \quad (4.8)$$

With this expression, the total intensity of diffracted waves at the central point along the exit face can be calculated for any value of y_s by using the formulas of § 3(D). The total intensity as a function of y_s, which corresponds to the intensity along the central line on a section topograph, is thus established. Two profiles corresponding respectively to $u_o = 0$ and 3 Å are shown in Fig. 10 where $x_s = 0$ mm and $\Phi = 0$. The first profile shows one fringe due to the thickness variation and the second one contains six extra fringes due to the vibration whose amplitude has a Gaussian envelope, $\exp(-\beta_5 y_s^2/2)$. Such profiles compared

with experimental images, *i.e.* with the fringe positions on the central line of section topographs, provide values of the vibration amplitude on the central line.

The precision of such profiles has to be discussed. Two error sources exist: on the one hand the neglect of the variation of the thickness and the vibration amplitude along the *ox* direction and on the other hand the validity of Kato's theory itself when the vibration amplitude is high ($u_o \approx 7$ Å). The examples shown below suggest that, for the present case, the last point is most important and an error corresponding to one half the fringe spacing, *i.e.* 0.3 Å when generously estimated, may be reached for high values of u_o.

(D) Experimental images and simulated images

The first experimental section topograph (Fig. 11*b*) was taken in the middle of the electrode on the resonator with $x_s = 2.07$ mm, and with a time phase $\Phi = \pi/4$. The excitation voltage V was 6.046 mV which implies a local vibration amplitude $u_o(x_s, y_s)|_{x_s=2.07, y_s=0.00}$ of about 1.61 Å for $Q \approx 1 \times 10^6$. Here, $u_o(x_s, y_s)$ cannot be determined precisely, because the value of the quality factor Q is only approximate and it can also vary with the room temperature. By taking the extra fringe positions from the central line of the experimental image, the vibration amplitude $u_o(x_s, y_s)$ was determined by comparison with the intensity profile $I(y_s)$ (Fig. 11*a*): $u_o(x_s, y_s)|_{x_s=2.07, y_s=0.00} = 1.35$ Å. With this value of $u_o(x_s, y_s)$, the simulation was performed by solving Takagi's equations with the *x*-dependent term for the vibration amplitude included in the deformation model (Fig. 11*c*). It can be seen that the extra fringe positions in the experimental image are reproduced either by the simulated image or by the intensity profile. This demonstrates the agreement between Kato's theory and Takagi's theory for the present case.

A second experimental image with a higher vibration amplitude is shown in Fig. 12(*b*) where

$x_s = 1.11$ mm, $\Phi = 0$ and the estimated value of $u_o(x_s, y_s)|_{x_s=1.11, y_s=0.00}$ was about 4.30 Å. As before, the determination by the intensity profile leads to $u_o(x_s, y_s)|_{x_s=1.11, y_s=0.00} = 4.80$ Å (Fig. 12*a*). The simulation (Fig. 12*c*) was performed by solving Takagi's equations and it was found that the image with a corrected value $u_o(x_s, y_s)|_{x_s=1.11, y_s=0.00} = 5.00$ Å reproduced the experimental fringe positions best. A small difference exists between the experimental image and the two calculations for the upper part of

Fig. 11. Comparison between intensity profile, experimental image and simulated image. (*a*) Intensity profile $I(y_s)$ using the values $x_s = 2.07$ mm, $\Phi = \pi/4$ and $u_o(x_s, y_s)|_{x_s=2.07, y_s=0.00} = 1.35$ Å. (*b*) Experimental image where $x_s = 2.07$ mm and $\Phi = \pi/4$. (*c*) Simulated image performed with the same values as in (*a*).
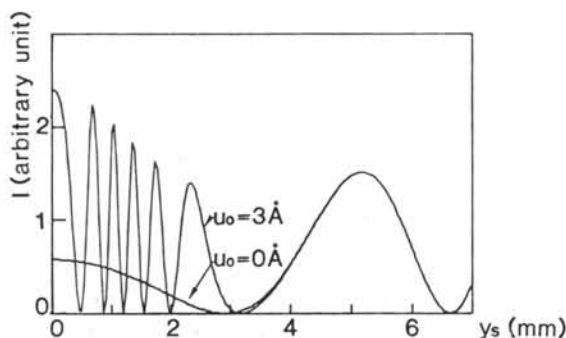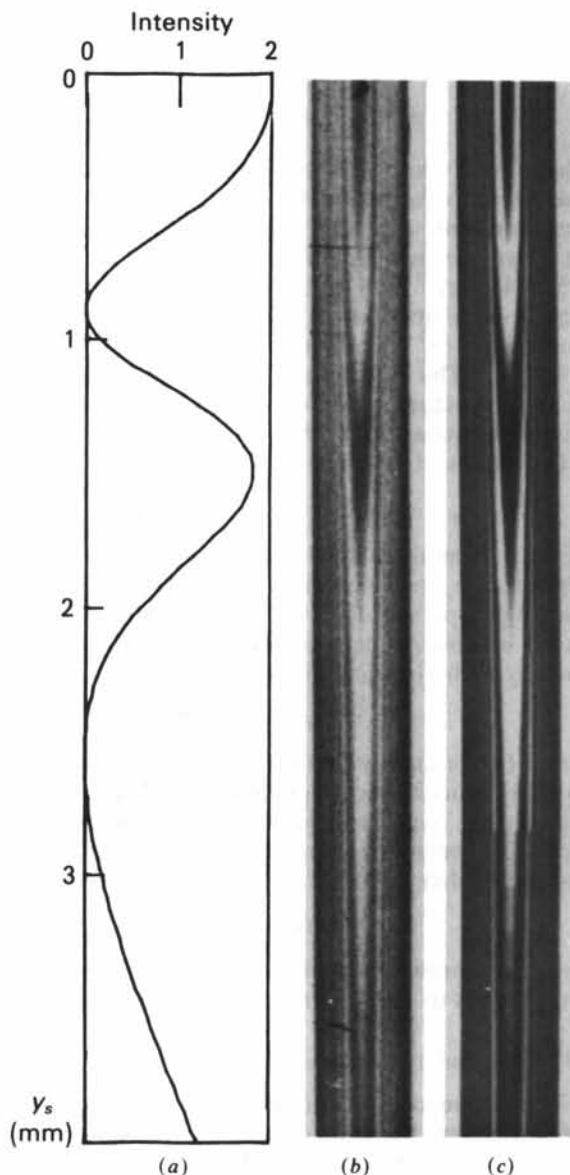
Fig. 10. Profile of the intensity $I(y_s)$ along the central line of a section topograph for a curved resonator where $x_s = 0$ mm and $\Phi = 0$. (*a*) $u_o = 0$ Å, perfect crystal; (*b*) $u_o = 3$ Å.

the section topograph where the vibration amplitude is high (about 5 Å). This is probably due to the experimental factors not taken into account such as saturation of the recording film, diffusion by air and polychromatism of the incident beam. Some asymmetry in fringe patterns with respect to the central line can also be seen in the experimental and simulated images. This fact is most pronounced on the experimental image. This asymmetry may suggest the

beginning of the vibration amplitude range where Kato's theory is becoming invalid. It is recalled that the validity range previously estimated in (3.2) is $u_o \leq 7$ Å.

These two examples show that extra *Pendellösung* fringes can be understood and analysed by Kato's theory for the range of vibration amplitudes which is roughly estimated by (3.2). It is important to note that the criterion (3.2) is applied locally. This means that for resonators operating at higher excitation levels, one can always apply Kato's theory for zones of low amplitudes and get vibration parameters. Such determination of acoustic characteristics by the *Pendellösung* fringe contour is useful for further work in order to analyse the influence of defects on the vibrational state which is one aim of the resonator study.

APPENDIX I

(A) Intensity

The intensity of the waves, or the energy transported along each trajectory, depends on the initial and final conditions of the trajectory:

$$I = \frac{\pi}{\Lambda_o} \frac{\cos \theta_a}{2 \sin 2\theta_B} \frac{(1-p_e)(1+p_a)}{(1-p_e^2)^{3/2}} \left| \frac{\delta p_e}{\delta a_a} \right|, \quad (I.1)$$

where the subscript e expresses the conditions at the entrance face and the subscript a those of the exit face. The last term represents the change in the trajectory cross section and it is given by the following formula. If the equation $F(x, z, p_e) = 0$ defines all the trajectories through the parameter p_e, then

$$\left| \frac{\delta a_a}{\delta p_e} \right| = \frac{|\partial F/\partial p_e|}{[(\partial F/\partial x)^2 + (\partial F/\partial z)^2]^{1/2}}. \quad (I.2)$$

(B) Anomalous absorption

$$B_i = \exp\left[\pm (\mu_g/\cos \theta_B) \int_{L_i} (1-p^2)^{1/2} \, dz \right] \quad (I.3)$$

where $i = 1, 2$ and the upper and lower signs are respectively for wavefield (1) and wavefield (2). L_i denotes the trajectory. μ_g is proportional to the imaginary part of $(\chi_g \chi_{\bar{g}})^{1/2}$ where χ_g is the g-order term in the Fourier expansion of the susceptibility.

APPENDIX II

(α) We want to show that only one trajectory passes through any point (x, z) inside the Borrmann triangle. When the trajectory equation (3.4) is
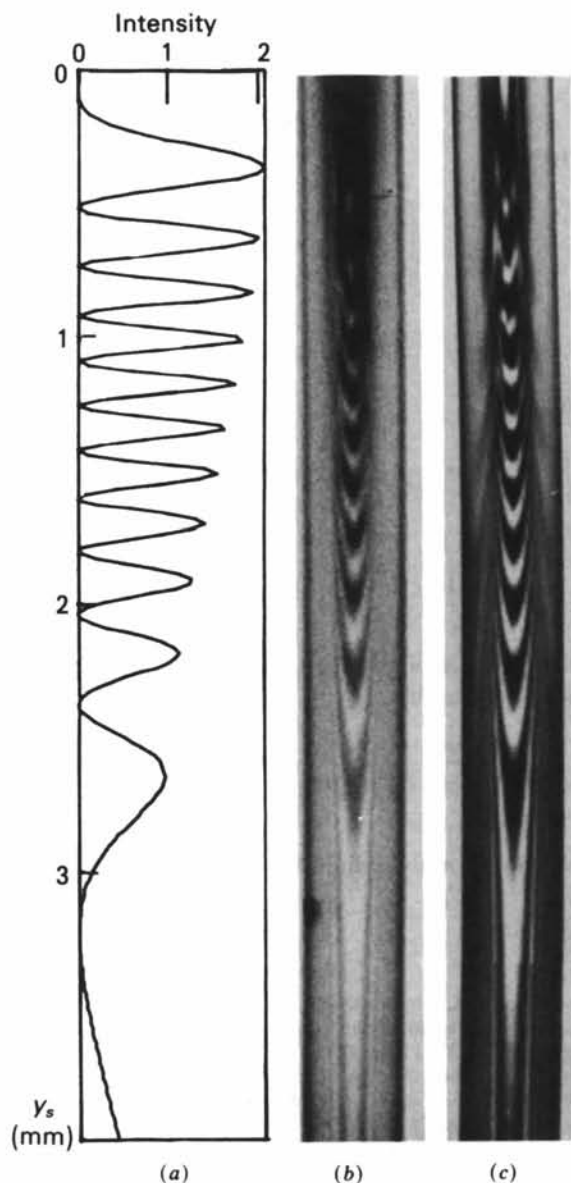

Fig. 12. Comparison between intensity profile, experimental image and simulated image. (a) Intensity profile $I(y_s)$ using the values $x_s = 1.11$ mm, $\Phi = 0$ and $u_o(x_s, y_s)|_{x_s=1.11, y_s=0.00} = 4.80$ Å. (b) Experimental image where $x_s = 1.11$ mm and $\Phi = 0$. (c) Simulated image performed with the same values of x_s and Φ as in (a) and a corrected value $u_o(x_s, y_s)|_{x_s=1.11, y_s=0.00} = 5.00$ Å.

rewritten as [for wavefield (1)]

$$F(x, z, a) = \int_0^{z/t} \frac{a - b \sin(n\pi\varphi)}{\{1 + [a - b \sin(n\pi\varphi)]^2\}^{1/2}} \, d\varphi - \frac{x}{ct} = 0$$

(II.1)

we shall know whether several values of a satisfy $F(x, z, a) = 0$ for a given point (x, z). This case can be eliminated because F is a monotonically increasing function of a:

$$\frac{\partial F}{\partial a} = \int_0^{z/t} \frac{d\varphi}{\{1 + [a - b \sin(n\pi\varphi)]^2\}^{3/2}} > 0.$$

(II.2)

The existence of a root can also be ensured by

$$F(x, z, a)|_{a \to -\infty} < 0 \quad \text{and} \quad F(x, z, a)|_{a \to +\infty} > 0.$$

(β) The inclination of the trajectory on the exit face is given by

$$p|_{z=t} = \frac{a \mp b \sin(n\pi z/t)}{\{1 + [a \mp b \sin(n\pi z/t)]^2\}^{1/2}}\bigg|_{z=t}$$

$$= \frac{a}{(1 + a^2)^{1/2}} = p_e.$$

(II.3)

(γ) If the trajectory L_1 of wave (1) is defined by its initial inclination $+p_e$ (or $+a$),

$$\frac{x_1}{ct} = \int_0^{z/t} \frac{a - b \sin(n\pi\varphi)}{\{1 + [a - b \sin(n\pi\varphi)]^2\}^{1/2}} \, d\varphi,$$

(II.4)

the trajectory L_2 of wave (2) defined by the opposite initial inclination $-p_e$ (or $-a$) has the expression

$$\frac{x_2}{ct} = \int_0^{z/t} \frac{-a + b \sin(n\pi\varphi)}{\{1 + [-a + b \sin(n\pi\varphi)]^2\}^{1/2}} \, d\varphi = -\frac{x_1}{ct}.$$

(II.5)

APPENDIX III

First, it is noted that

$$p_e = p_a = \frac{a}{(1 + a^2)^{1/2}}$$

and

(III.1)

$$\cos \theta_a = (1 + \tan^2 \theta_a)^{-1/2} = (1 + c^2 p_a^2)^{-1/2}.$$

The terms concerning the initial and final conditions of the trajectory are calculated as follows:

$$\frac{\cos \theta_a}{2 \sin 2\theta_B} \frac{(1 - p_e)(1 + p_a)}{(1 - p_e^2)^{3/2}}$$

$$= [4 \sin \theta_B \cos \theta_B (1 + c^2 p_e^2)^{1/2} (1 - p_e^2)^{1/2}]^{-1}.$$

(III.2)

The trajectory equation (3.4), when the left term is replaced, becomes

$$F[x, z, a(p_e)] = \int_0^{z/t} \frac{a - b \sin(n\pi\varphi)}{\{1 + [a - b \sin(n\pi\varphi)]^2\}^{1/2}} \, d\varphi$$

$$- \frac{x}{ct} = 0.$$

(III.3)

The cross section change is then given by

$$\left| \frac{\delta a_a}{\delta p_e} \right| = \frac{|\partial F/\partial a| \, da/dp_e}{[(\partial F/\partial x)^2 + (\partial F/\partial z)^2]^{1/2}}$$

$$\frac{\partial F}{\partial x}\bigg|_{z=t} = -\frac{1}{ct}, \quad \frac{\partial F}{\partial z}\bigg|_{z=t} = \frac{a}{t(1 + a^2)^{1/2}} = \frac{p_e}{t}$$

(III.4)

and

$$\frac{\partial F}{\partial a}\bigg|_{z=t} = \int_0^1 \{1 + [a - b \sin(n\pi\varphi)]^2\}^{-3/2} \, d\varphi,$$

$$\frac{da}{dp_e} = \frac{1}{(1 - p_e^2)^{3/2}};$$

thus

$$\left| \frac{\delta a_a}{\delta p_e} \right| = \frac{ct}{(1 - p_e^2)^{3/2}(1 + c^2 p_e^2)^{1/2}}$$

$$\times \int_0^1 \{1 + [a - b \sin(n\pi\varphi)]^2\}^{-3/2} \, d\varphi. \quad (III.5)$$

Finally, we obtain the intensity by putting together these two results:

$$I = \frac{\pi}{4\Lambda_o t \sin^2 \theta_B \int_0^1 \{1 + [a - b \sin(n\pi\varphi)]^2\}^{-3/2} \, d\varphi} \frac{1 - p_e^2}{}$$

(III.6)

and this formula is the same as (3.7) by replacing p_e by a.

References

ANDO, Y. & KATO, N. (1966). *Acta Cryst.* **21**, 284-285.
BALIBAR, F. (1968). *Acta Cryst.* **A24**, 666-676.
DYUBLIK, A. Y. (1986). *Phys. Status Solidi B*, **134**, 503-513.
HART, M. (1966). *Z. Phys.* **189**, 269-291.
KATO, N. (1963). *J. Phys. Soc. Jpn*, **18**, 1785-1791.
KATO, N. (1964). *J. Phys. Soc. Jpn*, **19**, 67-77, 971-985.
KATO, N. (1974). In *X-ray Diffraction*, pp. 389-434, edited by L. V. AZAROFF, R. KAPLOW, N. KATO, R. J. WEISS, A. J. C. WILSON & R. A. YOUNG. New York: McGraw-Hill.
KATO, N. & ANDO, Y. (1966). *J. Phys. Soc. Jpn*, **21**, 964-968.
KOHLER, R., MOHLING, W. & PEIBST, H. (1974). *Phys. Status Solidi B*, **61**, 173-180.
PENNING, P. & POLDER, D. (1961). *Philips Res. Rep.* **16**, 419-440.
POLIKARPOV, I. V. & SKADORV, V. V. (1987). *Phys. Status Solidi B*, **143**, 11-17.

STEVENS, D. S. & TIERSTEN, H. F. (1986). *J. Acoust. Soc. Am.* **79**, 1811–1826.

TAKAGI, S. (1962). *Acta Cryst.* **15**, 1311–1312.

TAKAGI, S. (1969). *J. Phys. Soc. Jpn,* **26**, 1239–1253.

TAUPIN, D. (1964). *Bull. Soc. Fr. Mineral. Cristallogr.* **87**, 469–511.

TIERSTEN, H. F. & SMYTHE, R. C. (1979). *J. Acoust. Soc. Am.* **65**, 1455–1460.

ZARKA, A., CAPELLE, B., DETAINT, J. & SCHWARTZEL, J. (1987). Proc. 41st Annu. Frequency Control Symp., 27–29 May 1987, Philadelphia, USA, pp. 236–240.

The Incommensurate Misfit Layer Structure of (SnS)₁.₁₇NbS₂, 'SnNbS₃'. I. A Study by Means of X-ray Diffraction

BY A. MEETSMA, G. A. WIEGERS,* R. J. HAANGE AND J. L. DE BOER

Laboratory of Inorganic Chemistry, Materials Science Center of the University, Nijenborgh 16, 9747 AG Groningen, The Netherlands

Abstract

$(SnS)_{1.17}NbS_2$, $M_r = 334.92$, is a compound with misfit layer structure consisting of two-atom-thick layers of SnS and three-atom-thick sandwiches of NbS_2 which alternate along the c axis. The lattices of SnS and NbS_2 both have C-centered orthorhombic unit cells which match along the b and c axes but not along the a axes. The unit cells and space groups are $a = 5.673 (1)$, $b = 5.750 (1)$, $c = 11.760 (1)$ Å, space group $C2mb$ (no. 39), $Z = 4$, for SnS; $a = 3.321 (1)$, $b = 5.752 (1)$, $c = 11.763 (1)$ Å, space group $Cm2m$ (no. 38), $Z = 2$, for NbS_2. From the ratio of the lengths of the a axes of the two parts of the complete structure ($5.673/3.321 = 1.708$ being irrational) one obtains a composition $(SnS)_{1.17}NbS_2$. The structure determination consisted of three parts: the structures of the SnS and NbS_2 parts separately and their relative position. Intensities were measured with Mo $K\alpha$ radiation ($\lambda = 0.71073$ Å) at $T = 293$ K, $\mu = 102.3$ cm⁻¹. For the SnS part $R_F = 0.088$ for 306 unique reflections; for the NbS_2 part $R_F = 0.031$ for 329 unique reflections (for both cases $0kl$ reflections excluded). The relative position of these two lattices was determined from the common reflections $0kl$: $R_F = 0.072$ for 98 reflections. The SnS part of the structure consists of deformed slices of SnS with a thickness of half the cell edge of (hypothetical) NaCl-type SnS. Each Sn atom is in this way coordinated by five sulfur atoms; four sulfur atoms are in a plane perpendicular to the c axis with SnS distances 2.74 (1) (1×), 2.913 (1) (2×) and 3.01 (1) Å (1×), whereas the fifth Sn–S bond with length 2.695 (9) Å is approximately along the c axis. The NbS_2 part of the structure is that of NbS_2-$2H$ with Nb in trigonal prisms of sulfur; the Nb–S distances are 2.473 (1) Å. From

refinement of the common $0kl$ reflections the relative y and z positions of the two sublattices were found; along the common a direction the lattices of SnS and NbS_2 are incommensurate.

Introduction

Compounds of assumed composition MTX_3 ($M =$ Sn, Pb; $T =$ Ti, V, Nb, Ta; $X =$ S, Se) have been known for a considerable time (Schmidt, 1970; Sterzel & Horn, 1970; van Maaren, 1972; Donohue, 1975). The crystals obtained by syntheses from the elements have an appearance suggesting a layered structure but owing to very easy plastic deformation it has so far not been possible to determine the structure. X-ray powder diffraction revealed teteragonal or pseudo-tetragonal unit cells with $a \approx 4$, $c \approx 12$ Å. We succeeded in growing single crystals by vapor transport using chlorine as transport agent. In this paper the determination of the misfit layer structure of 'SnNbS₃' is described; the composition of the compound turned out to be $(SnS)_{1.17}NbS_2$; it will be designated for brevity as 'SnNbS₃'.

Experimental

'SnNbS₃' could be grown as thin platelets with diameters up to about 5 mm. The black crystals are mechanically very soft and have a brilliant luster. The starting material was SnNbS₃ obtained by syntheses from the elements at 1123 K and the temperature gradient was 1113–1043 K; transport was to the low-temperature side of the quartz tube.

Structure determination

Single-crystal X-ray diffraction with an Enraf–Nonius CAD-4F diffractometer using monochromatized Mo

---

* Author to whom correspondence should be addressed.